Check for updates

View Article Online
View Journal

Chemical Science

Accepted Manuscript

This article can be cited before page numbers have been issued, to do this please use: K. Zhang, Z. Chen, S. jia, Y. Yao, H. Tian, Q. Deng, X. Wu, J. Li, S. Deng, S. Xie and Q. Zhang, *Chem. Sci.*, 2026, DOI: 10.1039/D6SC02521H.

Chemical Science

Volume 9
Number 1
7 January 2018
Pages 1-268

rsc.li/chemical-science

ISSN 2041-6539

ROYAL SOCIETY OF CHEMISTRY

EDGE ARTICLE
Xinjing Tang *et al.*
Caged circular siRNAs for photomodulation of gene expression in cells and mice

ROYAL SOCIETY OF CHEMISTRY

rsc.li/chemical-science

View Article Online
DOI: 10.1039/D6SC02521H

ARTICLE

A Saddle-Shaped OBO-Doped Nanographene: Facile Synthesis, Adaptive Double-Layer Assembly, and Enhanced Lewis Acidity

Received 00th January 20xx,
Accepted 00th January 20xx

DOI: 10.1039/x0xx00000x

Kaixin Zhang[‡,a,b], Zuo-Chang Chen[‡,a,d], Shuaipeng Jia[b], Yang-Rong Yao[c], Han-Rui Tian[a], Qing-Song Deng[a], Xue-Miao Wu[a], Jun Li[d], Shun-Liu Deng[a], Su-Yuan Xie[a,*] and Qianyan Zhang[a,*]

Current OBO-doped nanographenes (**NG**s) are predominantly planar, and the precise synthesis of curved OBO-doped **NG**s remains a challenge owing to their limited thermodynamic stability. Herein, we report a two-step synthesis of the first saddle-shaped OBO-doped **NG**s (**1a**-**1c**) built upon a corannulene core. Pristine **1a** exhibits reversible thermo-responsive behavior characteristic of a lower critical solution temperature (LCST)-type response. Single-crystal X-ray diffraction analysis combined with theoretical calculations reveal that these nanographenes adopt a saddle geometry. Notably, the incorporation of bulky triisopropylphenyl (TIPP) groups not only imporves thermodynamic stability but also enables **1c** to form ordered, adaptive bilayer assemblies in the solid state, inducing dramatic flattening of the corannulene core—a rare example of structure adaptation driven by supramolecular assembly rather than intramolecular steric effects. Crystallographic analyses further demonstrate that such geometric distortion increases the accessibility of boron centers. Consequently, the saddle-shaped topology imparts significantly enhanced Lewis acidity to these **NG**s, facilitating the first crystallographically characterized dual methanol coordination on the concave surface of a boron-doped nanographene. This work introduces a unique topological scaffold combining non-planarity, multi-heteroatom doping, and bilayer assembly, expanding the family of heteroatom-doped **NG**s with novel topologies.

Introduction

Nanographenes (**NG**s), as two-dimensional π-conjugated materials with tunable electronic and optical properties, have garnered immense attention in the past decades for their potential applications in field-effect transistors, light-emitting diodes, solar cells and electrocatalysts[1-5]. The structural topology of **NG**s—ranging from planar to curved (bowl-shaped, saddle-shaped, warped, or tubular)—plays a pivotal role in determining their physical and chemical behaviors, as curvature introduces intrinsic electronic polarization and modulates intermolecular interactions[1,6-8]. Corannulene, a classic curved polycyclic aromatic hydrocarbon (PAH) with a bowl-shaped structure, serves as an ideal building block for constructing curved **NG**s due to its inherent C_5 symmetry and ability to undergo regioselective functionalization[9-17]. In this field, chemists like Scott[12], Siegel[13], Itami[14,15] et. al. have made great contributions. However, the synthesis of curved **NG**s with well-defined non-hexagonal rings still remains a significant challenge, as the introduction of strained rings often leads to structural instability and synthetic uncontrollability[18-23].

Heteroatom doping has proven particularly effective for functionalizing **NG**s, offering enhanced stability and tunable electronic properties for organic electronic applications[24-27]. This approach has recently enabled the solution-phase synthesis of the largest NBN-doped triangulene by Miao and colleagues in 2021[28]. Recently, Liu and co-workers reported NBN-edged porous nanographenes with unusual frontier molecular orbital distribution[29]. Meanwhile, OBO-doping, in which B and O atoms form three-membered O–B–O linkages or integrated heterocyclic rings, has emerged as a promising approach to enhance the stability and tune the aromaticity, Lewis acidity, and intermolecular assembly of **NG**s[30-34]. For instances, in 2016, Müllen, Feng, and Wang et. al. reported OBO-doped bistetracene analogue with stable zigzag edges[30]. Wang and Yang independently developed OBO-doped triangulene in 2022[31,32] (Figure 1). Notably these previous studies on OBO-doped **NG**s have primarily focused on planar structures with low-strain six-membered rings, while saddle-shaped OBO-doped **NG**s with unique symmetry have rarely been reported. The incorporation of non-hexagonal rings (e.g., pentagons, heptagons) into OBO-doped **NG**s is of particular interest, as these rings induce curvature and create distinct electronic environments, yet their synthesis is hampered by the high strain energy associated with ring fusion[35-36].

---

[a] State Key Laboratory for Physical Chemistry of Solid Surfaces, iChEM (Collaborative Innovation Center of Chemistry for Energy Materials), Department of Chemistry, Xiamen University, Xiamen 361005, China.
[b] College of Chemical Engineering and Materials Science, Quanzhou Normal University, Quanzhou 362000, China.
[c] College of Chemistry, Chemical Engineering and Materials Science, and State Key Laboratory of Radiation Medicine and Protection, Soochow University, Suzhou, Jiangsu 215123, China.
[d] Department of Chemistry and Engineering Research Center of Advanced Rare-Earth Materials of the Ministry of Education, Tsinghua University, Beijing 100084, China.

† K. Zhang and Z.-C. Chen contributed equally to this work.

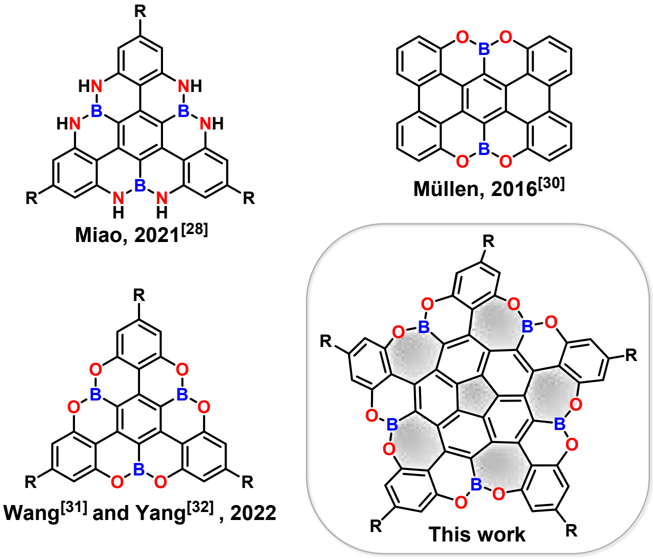

Fig. 1. Representative planar NBN-doped/OBO-doped **NG**s and novel saddle-shaped OBO-doped **NG**s in this work.

Another critical aspect of curved **NG**s is their self-assembly behavior. Due to the large contact area on both sides of the π-core, nanographenes typically tend to aggregation driven by dispersion forces[37-40]. Recently, self-assembly of nanographenes with a defined number of layers has garnered widespread interest[41-43]. However, the multilayer self-assembly of saddle-shaped **NG**s remain rather unexplored[44-45]. Controlling the self-assembly of saddle-shaped **NG**s into well-defined superstructures is essential for optimizing their collective properties, such as charge transport and light harvesting[46]. Additionally, the Lewis acidity of B-containing **NG**s enables coordination with nucleophiles (e.g., F^-, amines)[47-49], but coordination with weakly basic molecules like methanol has not been documented, representing an unexploited avenue to modulate their structural and optical properties.

Building on the versatile *sym*-1,3,5,7,9-pentakis(Bpin)corannulene platform[50], we herein report the synthesis of a unique family of saddle-shaped OBO-doped **NG**s (**1a**–**1c**) via a concise two-step route. These nanographenes feature a corannulene core fused with five heptagonal rings and five OBO-doped heterocyclic segments, representing the first example of B/O-doped **NG**s integrating five seven-membered rings. Pristine **1a** exhibits reversible thermo-responsive behavior. By introducing sterically demanding solubilizing groups (mesityl for **1b**, TIPP for **1c**), we achieved improved solubility and stability, thereby enabling the unambiguous structural characterization of a saddle-shaped OBO-doped **NG**. Remarkably, the **NG** (**1c**) undergoes adaptive self-assembles into a staggered bilayer structure, and its enhanced Lewis acidity allows for unique methanol coordination. This work not only enriches the synthetic methodology for curved heteroatom-doped **NG**s but also uncovers novel structure–property relationships, paving the way for the rational design of functional π-conjugated materials.

Results and discussion

View Article Online
DOI: 10.1039/D6SC02521H

Synthesis, Purification and Structural Characterization of Saddle-shaped OBO-Doped Nanographenes

Starting from *sym*-1,3,5,7,9-pentakis(Bpin)corannulene platform reported by Scott et al. (2012)[50], we developed a concise two-step route to OBO-doped nanographenes **1a**-**1c**. As depicted in Figure 2a, the OBO-doped nanographenes were synthesized via two principal steps. First, a five-fold coupling reaction between *sym*-1,3,5,7,9-pentakis(Bpin)corannulene and tailored aryl partners afforded cyclization precursors **2a**, **2b**, and **2c** in isolated yields of 72%, 66%, and 48%, respectively. Subsequently, BBr_3-mediated electrophilic borylation yielded target compounds **1a**, **1b**, and **1c** in yields of 52%, 23%, and 78%, respectively. The structures and symmetry of **1a**, **1b**, and **1c** were established by ^1H NMR spectroscopy (Figures S25-S39). All three compounds exhibit time-averaged C_5 symmetry in solution on the NMR timescale. For instance, **1c** displays two well-resolved singlets of equal intensity in the low-field region (Figure 2b), consistent with a highly symmetric architecture. The signal at 7.06 ppm is assigned to triisopropylphenyl protons (**Hc**), while the resonance at 7.18 ppm corresponds to skeletal protons **Ha** and **Hb**; the low-field shift of the latter arises from the extended conjugation effect within the scaffold. High-resolution matrix-assisted laser desorption ionization time-of-flight mass spectrometry (MALDI-TOF MS) confirmed the molecular compositions of **1a**, **1b**, and **1c** (Figures 2c and S20-S22), with observed *m/z* values matching simulated spectra. **1a** (calcd. for $C_{50}H_{15}B_5O_{10}$ [M]: 830.1125, found: 830.1154); **1b** (calcd. for $C_{95}H_{65}B_5O_{10}$ [M]: 1420.4988, found: 1420.5022); and **1c** (calcd. for $C_{125}H_{125}B_5O_{10}$ [M]: 1841.0157, found: 1841.0182). Notably, an additional signal at m/z = 3862.0360 was observed

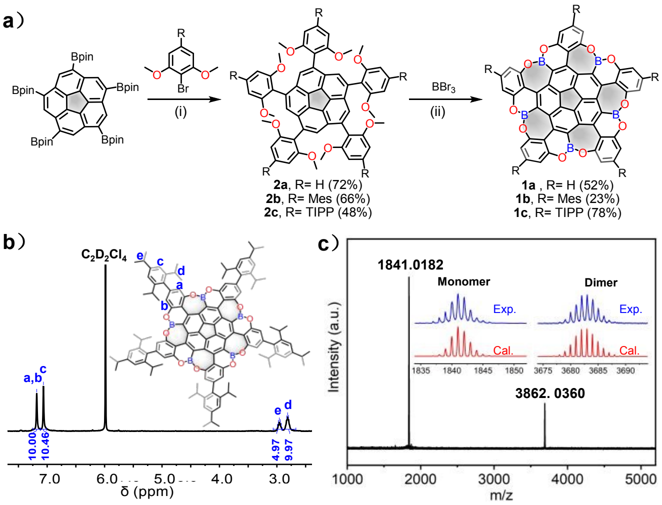

Fig. 2. Synthesis route, mass spectrometry and ^1H NMR spectrum of **1c**. (a) Reaction conditions: (i) For **2**: X-Phos, $Pd(PPh_3)_4$, Cs_2CO_3, DMF, 85°C (**2a**)/130°C (**2b** and **2c**), 12 h; (ii) For **1a-1c**: BBr_3, 150°C, 24h. (b) The ^1H NMR spectrum of **1c**. (c) The MALDI-TOF MS of **1c**.

View Article Online
DOI: 10.1039/D6SC02521H

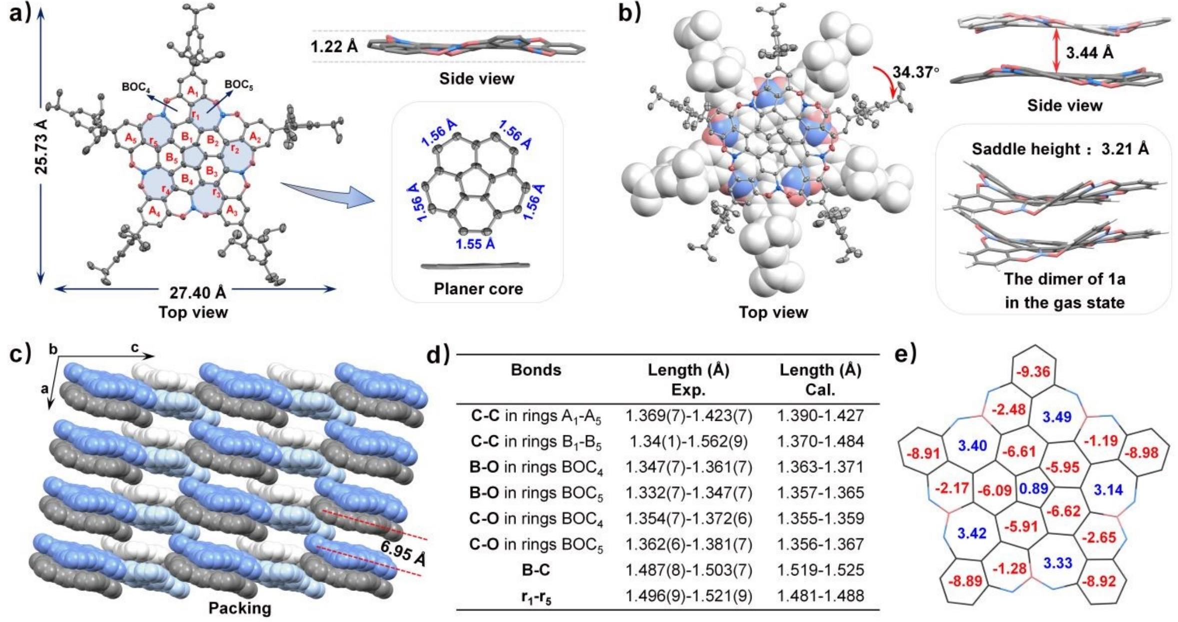

Bonds	Length (Å) Exp.	Length (Å) Cal.
C-C in rings A_1-A_5	1.369(7)-1.423(7)	1.390-1.427
C-C in rings B_1-B_5	1.34(1)-1.562(9)	1.370-1.484
B-O in rings BOC_4	1.347(7)-1.361(7)	1.363-1.371
B-O in rings BOC_5	1.332(7)-1.347(7)	1.357-1.365
C-O in rings BOC_4	1.354(7)-1.372(6)	1.355-1.359
C-O in rings BOC_5	1.362(6)-1.381(7)	1.356-1.367
B-C	1.487(8)-1.503(7)	1.519-1.525
r_1-r_5	1.496(9)-1.521(9)	1.481-1.488

Fig. 3. Single-crystal X-ray molecular structure and crystal packing arrangements of **1c** grown at 0 °C, with the NICS(1) values of **1c**. All hydrogen atoms and solvent molecules were omitted for clarity. (a) The single-molecule structure of **1c**, the top view (thermal ellipsoids of 30% probability), side view, corannulene core and bond lengths of corannulene rim in **1c**. Oxygen and boron were marked in pink and blue, respectively. (b) The dimer structure of **1c**, the top view (thermal ellipsoids of 30% probability) and side view. Oxygen and boron were marked in pink and blue, respectively. Inset: the gas-phase structure of the dimer of **1a**. (c) Molecular columnar packing arrangement (the triisopropylphenyl groups were omitted for clarity). (d) Bond lengths of the polycyclic framework of **1c**. (e) NICS(1) values of **1c** calculated at the B3LYP/6-31G(d,p) level.

for **1c**, consistent with the formation of a dimeric aggregate in the gas phase (Figure 2c).

Compound **1a** exhibits poor solubility in low-to-moderate polarity solvents (e.g. dichloromethane, toluene) but good solubility in highly polar solvents such as DMF and DMSO. This behavior can be rationalized by strong Lewis acid-base interactions between the boron centers and the polar donor solvents. Consistent with this picture, ^{11}B NMR spectra of **1b** and **1c** in DMSO-d_6 exhibit pronounced high-field shifts relative to those in $CDCl_3$ (Figures S34-S35, S40-S41), indicating the formation of tetracoordinate boron–solvent adducts. Similar solvent-dependent trends were observed in the absorption spectra of **1b** and **1c** (Figures S44-S45). Interestingly, heating the DMF solution of **1a** induced gradual precipitation, which reversed upon cooling—a thermo-reversible phase transition confirmed by variable-temperature ^{1}H NMR and dynamic light scattering (Figures S28 and S29). This behavior is characteristic of lower critical solution temperature (LCST)-type response[51], attributed to thermally weakened Lewis acid–base interactions between **1a** and DMF, allowing intermolecular π–π stacking to dominate and drive aggregation.

To improve the solubility in low-polar solvents, mesityl groups were incorporated to give **1b**, which indeed showed enhanced solubility in solvents such as dichloromethane and toluene. However, silica gel chromatography purification of **1b** led to significant yield loss (23%), likely due to its sensitivity toward weakly acidic surface sites. To address this stability issue, more sterically hindered triisopropylphenyl (TIPP) groups were installed to afford **1c**, which could be purified smoothly by silica gel chromatography in a high yield of 78%. The improved stability and processability of **1c** arise from the increased hydrophobic effect provided by the bulky isopropyl groups. Long-term solution stability studies further confirmed that **1c** is significantly more robust than **1b**.

Given the potential structural strain imposed by the combination of non-hexagonal rings and OBO-doping, single crystals of **1c** suitable for single-crystal X-ray diffraction (SCXRD) analysis were first grown via vapor diffusion (toluene/$CHCl_3$, 60 °C). The solid-state structure confirms a weak saddle-shaped topology composed of a central corannulene core surrounded by five heptagonal rings and five zigzag-edged segments. To the best of our knowledge, this represents the first example of a B/O-doped nanographene integrating five seven-membered rings. In contrast to planar OBO-doped nanographenes, **1c** exhibits a shallow saddle geometry with a saddle depth of 1.22 Å (Figure 3a)， which is significantly shallower than those observed for the gas-phase monomer (2.73 Å, Figure S61) and dimer (3.21 Å, Figure 3b) of **1a**. This phenomenon likely arises from intermolecular interaction forces among peripheral functional groups, which flatten the intrinsic saddle-shaped conformation characteristic of the unsubstituted skeletal framework. Remarkably, the crystal packing reveals a staggered bilayer arrangement (twist angle = 35.87°; Figure S8), effectively minimizing repulsion between TIPP groups. Such well-defined bilayer stacking is relatively uncommon among saddle-shaped **NG**s compared to their planar analogues. Due to slight disorder

View Article Online
DOI: 10.1039/D6SC02521H

in the core region, **1c** was recrystallized via slow evaporation at 0 °C, yielding highly ordered crystals (Figure 3a). The refined structure displays a discrete dimeric bilayer motif with a torsion angle of 34.37° and an interlayer distance of 3.44 Å (Figure 3b), indicative of moderate π-π interactions. Similar to the previously reported multilayer stacking mode of nanographene[52-53], this system rotates around the quasi-C_5 axis to accommodate the bulky groups. In addition, an inter-dimer distance of 6.95 Å, sufficiently large to suppress significant π–π interactions between adjacent dimers due to steric shielding.

Detailed structural analysis of this double-layer assembly revealed an unexpected flattening of the corannulene core in **1c**. The distance between the pentagon center and the mean plane of the rim atoms is only 0.02 Å—dramatically smaller than that of pristine corannulene (0.87 Å)[54-55] and previously reported warped nanographenes (0.37 Å)[15]. In contrast to earlier examples of core flattening driven by intramolecular steric repulsion between peripheral substituent[56-57], the planarization observed here is attributed to adaptive double-layer self-assembly. Density functional theory (DFT) calculations support this cooperative structural adaptation, revealing a simultaneous reduction in both bowl depth and saddle height upon dimerization (Figures S64 and S65). Notably, such flattening is absent in the optimized structure of **1a** (Figures S62 and S63), highlighting the critical role of the bulky TIPP groups in directing the double-layer assembly. Furthermore, dimers of **1c** exhibit columnar stacking along the *c*-axis, stabilized by inter-dimer C-H⋯π interactions (Figure 3c).

Aromaticity was evaluated through bond-length analysis and NICS(1) calculations (Figures 3d and 3e). The outer benzene rings (A_1-A_5) show bond-length equalization (1.369(7)-1.423(7) Å) and strongly negative NICS(1) values (-8.89 to -9.36), confirming their aromatic character. In contrast, all the heptagons and the hexagons constructed by OBO units are nonaromatic, as evidenced by the NICS(1) values: the BOC_5 rings exhibit slightly positive values, while the BOC_4 rings display only marginally negative values (Figure 3e). The B-O bond lengths in BOC_4 (1.347(7)-1.361(7) Å) and BOC_5 rings (1.332(7)-1.347(7) Å) are shorter than those in OBO-doped planar nanographenes (1.378-1.440 Å)[31,32] and other OBO-doped PAHs[30,58,59]. This shortening results in enhanced π-donation from oxygen to boron. Elongated bonds in the corannulene rim (~1.56 Å) relative to gas-phase optimized structures (~1.44 Å) may result from planarization-induced strain. Anisotropy of the induced current density (ACID) calculations further support these findings, revealing a pronounced clockwise diatropic ring current in rings A_1-A_5, indicative of their aromatic nature (Figure S71). However, the current appears disrupted at the B-O bonds in the ACID plots, which does not meet the criteria for antiaromaticity. Therefore, the aromaticity of BOC_5 ring is described as non-aromatic, which is also consistent with the NICS(1) calculation. In addition, as the OBO unit sites at the junction of the heptagon (BOC_5) and hexagon (BOC_4), the angle of ∠OBO is compressed to 110.01~111.61° (Table S2), smaller than the 120° required for ideal sp^2 hybridization. This geometric distortion disrupts the intrinsic three-center four-electron aromaticity of the OBO motif and renders the vacant boron orbitals more accessible for external Lewis base coordination.

Dimer Interaction Energy Analysis

To quantify the non-covalent interactions governing dimer formation, fragmentation-based energy calculations[60] were performed on the theoretically optimized dimers of **1a**, **1b** and **1c**. As shown in Figure 4, the dimer binding energy of **1c** (-127.13 kcal·mol^{-1}) is significantly stronger than those of **1a** (-62.13 kcal·mol^{-1}) and **1b** (-97.28 kcal·mol^{-1}). Control analysis indicates that the π–π interactions between the conjugated backbones are comparable across the series, implying that the energetic difference arises mainly from substituent effects. Large dispersion interaction in XEDA II (Figure S66) indicates that the dimer stability of **1c** is dominated by London dispersion forces, originating from strong instantaneous dipole–dipole attractions between polarizable electron clouds, typical for nonpolar/weakly polar systems. The exceptional stability of the **1c** dimer can be attributed to a synergistic combination of non-covalent forces: (i) π-π stacking between the curved conjugated backbones, (ii) C-H⋯π interactions among the bulky TIPP substituents, and (iii) C-H⋯O contacts between the alkyl substituents and the oxygen atoms of the OBO units.

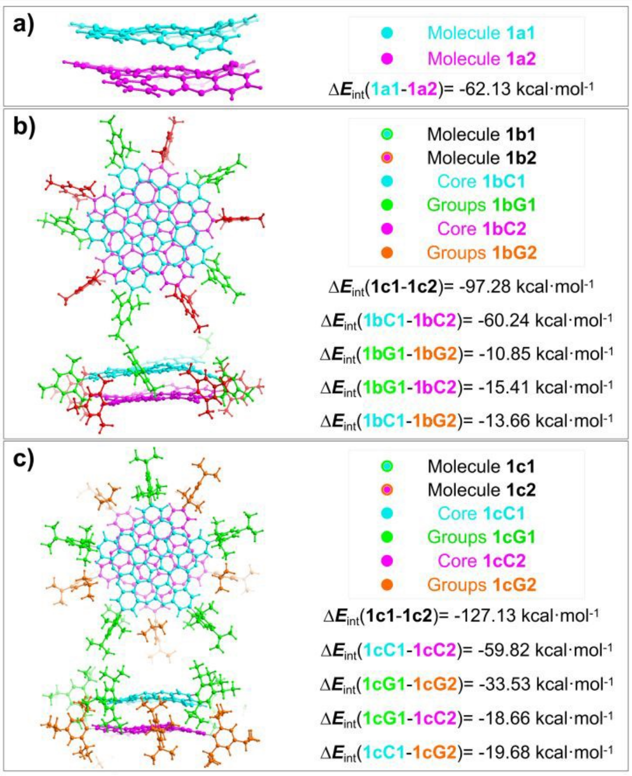

Fig. 4. Interaction energy analysis for dimer of **1** using fragmentation methods. (a) the dimer of **1a**, (b) the dimer of **1b** and (c) the dimer of **1c**.

Optical Properties and Electronic Structures of saddle-shaped OBO-doped nanographenes

The UV/Vis absorption and fluorescence spectra of compounds **1b** and **1c** were recorded in dilute dichloromethane solutions. Both compounds exhibit well-resolved vibronic bands with prominent absorption features spanning 300-520 nm

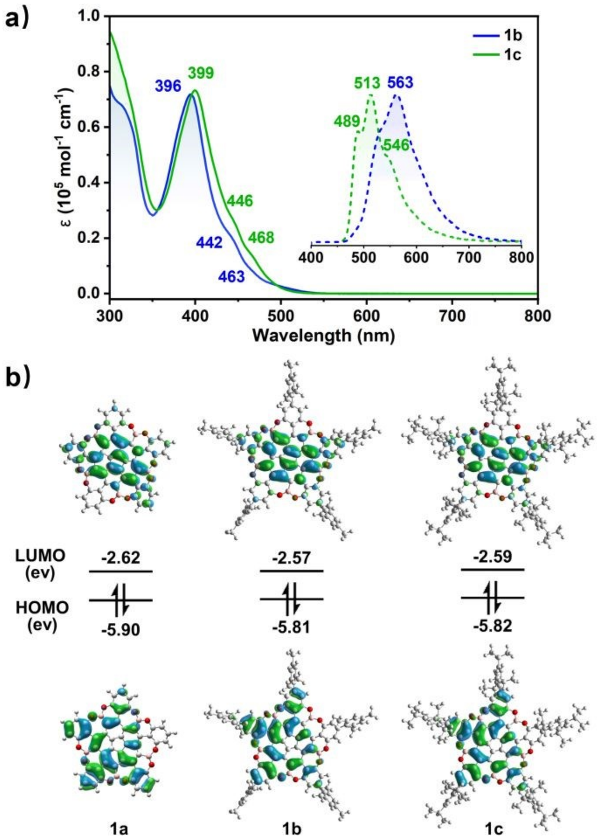

Fig. 5. Optical spectra (recorded in dichloromethane, 10 μM) and molecular orbitals. (a) UV/vis spectra of **1b** and **1c** are presented, with an inset photograph in the right corner displaying the emission spectra of **1b** and **1c** (represented by blue and green dotted lines, respectively). (b) Molecular orbitals of **1a**, **1b** and **1c.**

(Figure 5a), demonstrating a pronounced red shift compared to *sym*-pentaphenylcorannulene[50] and related OBO-doped triangulenes[31,32], consistent with an extended conjugation. Specifically, **1b** shows a maximum absorption at 396 nm with shoulders at 442 and 463 nm, whereas **1c** displays a slightly red-shifted profile with maxima at 399, 446, and 468 nm. This subtle difference can be attributed to the slightly stronger electron-donating effect of the TIPP groups in **1c** relative to the mesityl groups in **1b**, which subtly modulates the frontier orbital energies. Time-dependent density functional theory calculations reproduce the experimental trend, with transition energies of 3.28 eV for **1a,** 3.24 eV for **1b** and 3.23 eV for **1c** (Figure 5b), all lower than that of corannulene. The low-energy absorption bands are assigned to HOMO→LUMO transitions (Figures S68-S70 and Tables S6-S8), consistent with the observed blue shift of **1b** relative to **1c**. Moreover, the exceptionally small oscillator strengths of **1a**, **1b** and **1c** (0.0137, 0.0229 and 0.0254, respectively) further corroborate the weakly allowed and partially forbidden nature of their lowest excited states. The corresponding molar extinction coefficients (ε_max) were determined to be 7.21 × 10^4 M^{-1} cm^{-1} for **1b** and 7.35 × 10^4 M^{-1} cm^{-1} for **1c**. Emission maxima occurred at 563 nm (**1b**) and 513 nm (**1c**), with Stokes shifts of 100 nm and 45 nm, respectively. Transient photoluminescence analysis yielded quantum yields (Φ) and emission lifetimes (τ) as follows: **1a** (Φ = 2.4%, τ = 3.1 ns), **1b** (Φ = 11.5%, τ = 3.6 ns), **1c** (Φ = 14.4%, τ = 4.3 ns) (Figures S49-S51).The fluorescence quantum yield of **1** is relatively low compared to those of OBO-doped triangulenes (31-58%)[31,32], likely due to enhanced vibrational relaxation in the flexible saddle-shaped framework.

The higher fluorescence quantum yield of **1c** compared to **1b** can be rationalized by the steric restriction imposed by the bulky TIPP groups, which hinder the fast rotation of peripheral aromatic rings. This restriction suppresses non-radiative decay (2.39 × 10^8 s^{-1} for **1b**, 1.99 × 10^8 s^{-1} for **1c**) and enhances radiative decay (3.10 × 10^7 s^{-1} for **1b**, 3.35 × 10^7 s^{-1} for **1c**, Table S4). In contrast, the mesityl groups in **1b** rotate more freely. The constrained geometry also reduces structural relaxation upon excitation, minimizing the difference between ground- and excited-state geometries and thus reducing the Stokes shift. Electrochemically, both **1b** and **1c** exhibit quasi-reversible reduction waves in cyclic voltammetry (CV), with half-wave potentials ($E_{1/2}^{red1}$) at −1.42 V and −1.40 V (Figure S52), respectively, in agreement with the trend in calculated LUMO energies.

Lewis Acidity and Dual Methanol Coordination

To evaluate Lewis acidity and binding behaviors of boron atoms, titrations of **1b** and **1c** with tetrabutylammonium fluoride (TBAF) in tetrahydrofuran (THF) were performed, leading to dramatic changes in absorption and emission spectra. New absorption bands emerged at 352 and 382 nm for **1b** and 341 and 375 nm for **1c**, accompanied by overall blue shifts of the spectra (Figures S53-S54), along with distinct emission color changes (Figure S58). However, non-linear curve-fitting analyses did not yield consistent or chemically reasonable binding stoichiometries (Table S5), suggesting that fluoride binding under these conditions does not follow a simple 1:1 or 1:2 model but involves more complex cooperative or multisite binding.

Intriguingly, slow diffusion of methanol vapor into a chloroform solution of **1c** afforded single crystals of a well-defined methanol-coordinated adduct, **$2CH_3OH·1c$**, which was fully characterized by SCXRD (Figure 6a). The solid-state structure confirms tetracoordinate boron centers, with two methanol molecules selectively bound to two boron sites on the concave face of the saddle (Figure S9). To our knowledge, this represents the first documented case of methanol coordination in a boron-doped nanographene. Although molecular dimensions remain similar to **1c**, methanol binding induces a dramatic structural adaptation: the saddle height increases from 1.22 Å to 2.45 Å, and the corannulene core reverts to a distinct curved bowl geometry (depth = 0.59 Å). The B–O bond distances of 1.563(8) Å and 1.57(1) Å are characteristic of dative bonds, markedly longer than covalent B–O bonds in methoxide complexes and consistent with calculated values (Figure S78). This coordination also reduces OBO bond angles (Table S2) and amplifies negative curvature of the heptagonal rings, with curvature parameters ($k(v)$)[18] approximately double (Figures 6b and S19) those of fluoride-coordinated analogues[41-43], indicating greater distortion. In the solid state, **$2CH_3OH·1c$**

View Article Online
DOI: 10.1039/D6SC02521H

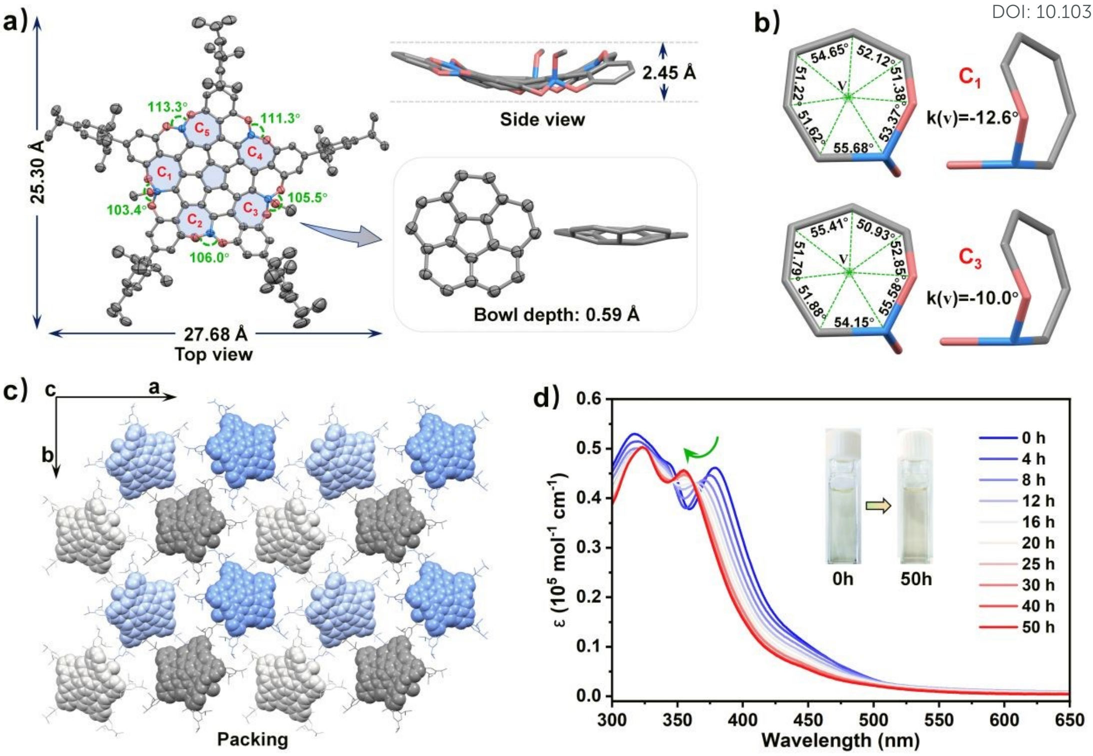

Fig. 6. Single-crystal X-ray molecular structure, crystal packing arrangements and time-dependent UV/vis spectra of **$2CH_3OH\cdot 1c$.** (a) the top view (thermal ellipsoids of 30% probability), side view of **$2CH_3OH\cdot 1c$**, and the corannulene core in the crystal structure (thermal ellipsoids of 30% probability). (b) The methoxy-coordinated heptagons in the crystal structures, with the centroid shown as a green ball. (c) crystal packing arrangements. All hydrogen atoms and solvent molecules were omitted for clarity. (d) Time-dependent UV/vis spectra of **1c** (8.2 μM) in methanol solution. The zero-time point for spectral acquisition was defined as the moment to start testing immediately after dissolution.

forms a herringbone arrangement along the *b*-axis (layer spacing = 7.34 Å), stabilized by C-H⋯π interactions (Figures 6c and S12).

Computational scanning of possible **$2CH_3OH\cdots 1c$** and **$4CH_3OH\cdots 1c$** isomers showed very small energy differences, suggesting the coexistence of multiple coordination isomersin solution. Notably, the crystallographically characterized isomer (**$2CH_3OH\cdots 1c$-1**) was identified as the most stable among the **$2CH_3OH\cdots 1c$** series (Figure S78). Furthermore, calculations simulating the stepwise addition of 1–5 methanol molecules to **1c** indicate that stable coordination complexes are formed with three to four methanol molecules, as the incremental binding energy drops significantly for the fifth methanol, ($|\Delta \boldsymbol{E}_{\text{int}}(\text{inc})| \approx$ 5.04 kcal·mol^{-1}; Figure S77). Moreover, as the number of methanol molecules increases, the coordination bond lengths between methanol and **1c** ($r_{\text{O}\cdots\text{B}}$) gradually converge to the values observed in the crystallographic data (Figure S80).

The dynamics of methanol coordination were probed experimentally. Titrations of **1c** with methanol in dichloromethane, monitored by ^{1}H-NMR and UV/vis spectroscopy (Figures S59-S60), revealed negligible changes in chemical shifts and only minor spectral variations. However, time-dependent UV/vis spectra in pure methanol revealed a gradual blue shift over time (Figure 6d), demonstrating that the coordination process is thermodynamically favorable but kinetically slow. DFT calculations of **1c** with 1~5 methanol molecules in a solvation model reproduced this spectral blue-shifting trend (Figures 6d and S76), validating the sequential coordination mechanism.

Finally, the Lewis acidity of **1c** was compared with that of planar OBO-doped triangulene analogue[31,32] via coordination energy calculations (Figure S81). The results clearly indicate that enhanced Lewis acidity in saddle-shaped OBO-nanographene **1c**, supported by its lowered LUMO level and stronger calculated binding energy toward methanol. This enhanced Lewis acidity can be attributed to the reduced steric shielding around the boron centers in the curved scaffold (Figure S13, OBCC torsion angles in BOC_4 or BOC_5 rings: 0.05~17.51°), in contrast to the more congested environment in planar analogues (OBCC torsion angles in BOC_4 rings: 0.42~1.52°)[31,32].

Conclusions

In summary, we have designed and synthesized a unique family of saddle-shaped OBO-doped nanographenes based on a corannulene core fused with five heptagonal rings, via a concise two-step synthetic strategy. Although DFT calculation calculations predict a typical saddle-shaped geometry, single-crystal X-ray diffraction analysis reveals that these curved nanographenes adopt a shallow saddle geometry, and unexpectedly form ordered adaptive double-layer assemblies in the solid state. Notably, such bilayer packing induces a dramatic flattening of the corannulene core, which is distinct from previously reported sterically driven planarization and represents a rare example of structure adaptation driven by supramolecular assembly.

These saddle-shaped nanographenes exhibit structure-dependent solubility, thermo-responsive behavior, and tunable optical and electronic properties. The bulky triisopropylphenyl substituents significantly enhance stability, solubility, and dimer-binding energy through synergistic non-covalent interactions. Aromaticity analyses reveal that the outer benzene rings maintain strong aromaticity, while the OBO-containing heterocyclic units are rendered non-aromatic due to geometric distortion, which in turn increases the accessibility of the boron centers. Benefiting from the unique curved topology, these OBO-doped nanographenes display enhanced Lewis acidity and enable the rare crystallographic observation of dual methanol coordination on the concave surface. This work not only expands the structural diversity of heteroatom-doped curved nanocarbons but also establishes a direct link between three-dimensional molecular topology, adaptive supramolecular assembly, and Lewis acid functionality, offering a new design principle for functional polycyclic aromatic materials.

Author contributions

Q. Zhang and S.-Y. Xie conceived of the idea and directed the research. K. Zhang designed the protocols, performed the experiments, and analyzed the data. Z.-C. Chen and J. Li conducted density functional theory calculations. Q.-S. Deng and X.-M. Wu participated in organic synthesis. S. Jia, Y.-R. Yao and H.-R. Tian performed X-ray crystallography. K. Zhang, Q. Zhang and S. Jia wrote the manuscript. Q. Zhang, S.-Y. Xie, and S.-L. Deng coordinated and supervised the project. All authors discussed the results and revised the manuscript.

Conflicts of interest

There are no conflicts to declare.

Data availability

Crystallographic data for the structures reported in this article have been deposited at the Cambridge Crystallographic Data Centre, under deposition number 2486275 (**1c** at 0 °C), number 2486277 (**1c** at 60 °C), number 2486279 (**$2CH_3OH·1c$** at 0 °C). Copies of the data can be obtained free of charge via https://www.ccdc.cam.ac.uk/structures/. The experimental data and the characterization data are available in the Supplementary Information. All relevant data that support the findings of this work are available from the corresponding author on request. The atomic coordinates of the optimized computational model data generated in this study are provided in the Source Data file. Source data are provided with this paper.

Acknowledgements

View Article Online
DOI: 10.1039/D6SC02521H

We thank National Natural Science Foundation of China (NSFC) (22271238, 22571264, 92361303, 22305200, 22301249 and 21721001) for support.

References

1 A. Narita, X.-Y. Wang, X. Feng and K. Müllen, *Chem. Soc. Rev.*, 2015, **44**, 6616-6643.
2 B. Wu, H. Meng, X. Chen, Y. Guo, L. Jiang, X. Shi, J. Zhu, J. Long, W. Gao, F. Zeng, W.-J. Jiang, Y. Zhu, D. Wang and L. Mai, *Angew. Chem., Int. Ed.*, 2025, **64**, e202415071.
3 Z. Liu, S. Fu, X. Liu, A. Narita, P. Samorì, M. Bonn, and H. I. Wang, *Adv. Sci.*, 2022, **9**, 2106055.
4 Y. Gu, Z. Qiu and K. Müllen, *J. Am. Chem. Soc.*, 2022, **144**, 11499-11524.
5 Y., Zhu and M. A. Petrukhina, *Chem. Soc. Rev.*, 2026, **55**, 3061-3077.
6 T. Enoki, Y. Kobayashi and K.-I. Fukui, *Int. Rev. Phys. Chem.*, 2007, **26**, 609-645.
7 P., Izquierdo-García, J., Lión-Villar, J. M. Fernández-García and N. Martín, *Chem. Soc. Rev.*, 2025, **54**, 11089-11104.
8 S. Mishra, D. Beyer, K. Eimre, S. Kezilebieke, R. Berger, O. Gröning, C. A. Pignedoli, K. Müllen, P. Liljeroth, P. Ruffieux, X. Feng and R. Fasel, *Nat. Nanotechnol.*, 2020, **15**, 22-28.
9 W. E. Barth and R. G. Lawton, *J. Am. Chem. Soc.*, 1966, **88**, 380.
10 X. Li, F. Kang and M. Inagaki, *Small*, 2016, **12**, 3206.
11 M. C. Stuparu, *Acc. Chem. Res.*, 2021, **54**, 2858.
12 V. M. Tsefrikas and L. T. Scott, *Chem. Rev.*, 2006, **106**, 4868.
13 A. M. Butterfield, B. Gilomen and J. S. Siegel, *Org. Process Res. Dev.*, 2012, **16**, 664.
14 K. Kato, Y. Segawa, L. T. Scott and K. Itami, *Angew. Chem. Int. Ed.*, 2018, **57**, 1337-1341.
15 K. Kawasumi, Q. Zhang, Y. Segawa, L. T. Scott and K. Itami, *Nat. Chem.*, 2013, **5**, 739-744.
16 K. Shoyama and F. Würthner, *J. Am. Chem. Soc.*, 2019, **141**, 13008-13012.
17 Z.-Z. Zhu, Z.-C. Chen, Y.-R. Yao, C.-H. Cui, S.-H. Li, X.-J. Zhao, Q. Zhang, H.-R. Tian, P.-Y. Xu, F.-F. Xie, X.-M. Xie, Y.-Z. Tan, S.-L. Deng, J. M. Quimby, L. T. Scott, S.-Y. Xie, R.-B. Huang and L.-S. Zheng, *Sci. Adv.*, 2019, **5**, eaaw0982.
18 S. H. Pun and Q. Miao, *Acc. Chem. Res.*, 2018, **51**, 1630-1642.
19 W. Niu, J. Ma and X. Feng, *Acc. Chem. Res.*, 2022, **55**, 3322-3333.
20 Q. Zhang, T. Liu, Z. Gan, Y.-Z. Tan and S.-Y. Xie, *Acc. Mater. Res.*, 2025, **6**, 1476–1489.
21 Chaolumen, I. A. Stepek, K. E. Yamada, H. Ito and K. Itami, *Angew. Chem., Int. Ed.*, 2021, **60**, 23508-23532.
22 I. R. Márquez, S. Castro-Fernández, A. Millán and A. G. Campaña, *Chem. Commun.*, 2018, **54**, 6705-6718.
23 J. Spengler, Y. Wagenhäuser, M. Kuhstrebe and F. Würthner, *J. Am. Chem. Soc.*, 2026, **148**, 9014-9022.
24 A. Borissov, Y. K. Maurya, L. Moshniaha, W.-S. Wong, M. Żyła-Karwowska and M. Stępień, *Chem. Rev.*, 2022, **122**, 565-788.
25 S. Madayanad Suresh, D. Hall, D. Beljonne, Y. Olivier and E. Zysman-Colman, *Adv. Funct. Mater.*, 2020, **30**, 1908677.
26 X.-Y. Wang, X. Yao, A. Narita and K. Müllen, *Acc. Chem. Res.*, 2019, **52**, 2491-2505.
27 A. Nowak-Król, P. T. Geppert and K. R. Naveen, *Chem. Sci.*, 2024, **15**, 7408-7440.
28 M. Zhao and Q. Miao, *Angew. Chem., Int. Ed.*, 2021, **60**, 21289-21294.
29 Y. Yu, A. Izu, J. M. Marín Beloqui, S. Rana, K. S. Mali, S. De Feyter, D. Casanova, J. Casado and J. Liu, *J. Am. Chem. Soc.*, 2025, **147**, 20098-20108.

View Article Online
DOI: 10.1039/D6SC02521H

30 X.-Y. Wang, A. Narita, W. Zhang, X. Feng and K. Müllen, *J. Am. Chem. Soc.*, 2016, **138**, 9021-9024.

31 C. Chen, J. Lu, Y. Lv, Y. Yan, Q. Sun, A. Narita, K. Müllen and X.-Y. Wang, *Angew. Chem., Int. Ed.*, 2022, **61**, e202212594.

32 X. Chen, D. Tan, J. Dong, T. Ma, Y. Duan and D.-T. Yang, *J. Phys. Chem. Lett.*, 2022, **13**, 10085-10091.

33 A. S. Scholz, M. Bolte, A. Virovets, E. Peresypkina, H.-W. Lerner, C. S. Anstöter and M. Wagner, *J. Am. Chem. Soc.*, 2024, **146**, 12100-12112.

34 A. Kinikar, X.-Y. Wang, M. Di Giovannantonio, J. I. Urgel, P. Liu, K. Eimre, C. A. Pignedoli, S. Stolz, M. Bommert, S. Mishra, Q. Sun, R. Widmer, Z. Qiu, A. Narita, K. Müllen, P. Ruffieux and R. Fasel, *ACS Nanosci. Au*, 2024, **4**, 128-135.

35 H. Lv, K. Xiang and D.-T. Yang, *Eur. J. Org. Chem.*, 2022, e202201208.

36 H. Luo and J. Liu, *Angew. Chem., Int. Ed.*, 2024, **63**, e202410759.

37 L. Zhang, Y. Cao, N. S. Colella, Y. Liang, J.-L. Brédas, K. N. Houk and A. L. Briseno, *Acc. Chem. Res.*, 2015, **48**, 500-509.

38 S. Ito, M. Wehmeier, J. D. Brand, C. Kübel, R. Epsch, J. P. Rabe and K. Müllen, *Chem. Eur. J.*, 2000, **6**, 4327-4342.

39 Z. Zhang, D. Csókás, I. Fernández and M. C. Stuparu, *Chem*, 2024, **10**, 3199-3211.

40 Y. Gao, Z. Liu, T. Li and W. Zhao, *Angew. Chem., Int. Ed.*, 2023, **62**, e202314006.

41 Z.-L. Qiu, Y. Cheng, Q. Zeng, Q. Wu, X.-J. Zhao, R.-J. Xie, L. Feng, K. Liu and Y.-Z. Tan, *J. Am. Chem. Soc.*, 2023, *145*, 3289-3293.

42 M. A. Niyas, K. Shoyama, M. Grüne and F. Würthner, *Nature*, 2025, **637**, 854-859.

43 S. Soldner, K. Shoyama, M. Stolte and F. Würthner, *Angew. Chem., Int. Ed.*, 2026, **65**, e2434302.

44 K. Ikemoto, M. Akiyoshi, T. Mio, K. Nishioka, S. Sato and H. Isobe, *Angew. Chem., Int. Ed.*, 2022, **61**, e202204035.

45 K. Kato, K. Takaba, S. Maki-Yonekura, N. Mitoma, Y. Nakanishi, T. Nishihara, T. Hatakeyama, T. Kawada, Y. Hijikata, J. Pirillo, L. T. Scott, K. Yonekura, Y. Segawa and K. Itami, *J. Am. Chem. Soc.*, 2021, **143**, 5465-5469.

46 K. Zhang, P. A. Hope, M. El Bitar Nehme, A. Linden, B. Spingler and M. Rickhaus, *Chem. Eur. J.*, 2023, **29**, e202203954.

47 S. Osumi, S. Saito, C. Dou, K. Matsuo, K. Kume, H. Yoshikawa, K. Awaga and S. Yamaguchi, *Chem. Sci.*, 2016, **7**, 219-227.

48 Y. Min, C. Dou, D. Liu, H. Dong and J. Liu, *J. Am. Chem. Soc.*, 2019, **141**, 17015-17021.

49 C. Maeda, S. Michishita, I. Yasutomo and T. Ema, *Angew. Chem., Int. Ed.*, 2025, **64**, e202418546.

50 M. N. Eliseeva and L. T. Scott, *J. Am. Chem. Soc.*, 2012, **134**, 15169-15172.

51 S. Ma, Y. Zhu, W. Dou, Y. Chen, X. He and J. Wang, *Sci. China Chem.*, 2021, **64**, 576-580.

52 B. Pigulski, K. Shoyama, M.-J. Sun and F. Würthner, *J. Am. Chem. Soc.*, 2022, **144**, 5718-5722.

53 M. Mahl, M. A. Niyas, K. Shoyama and F. Würthner, *Nat. Chem.*, 2022, **14**, 457-462.

54 J. C. Hanson and C. E. Nordman, *Acta Crystallogr. Sect. B*, 1976, **32**, 1147.

55 M. A. Petrukhina, K. W. Andreini, J. Mack and L. T. Scott, *J. Org. Chem.*, 2005, **70**, 5713-5716.

56 Q. Zhang, K. Kawasumi, Y. Segawa, K. Itami and L. T. Scott, *J. Am. Chem. Soc.*, 2012, **134**, 15664-15667.

57 E. Solel, D. Pappo, O. Reany, T. Mejuch, R. Gershoni-Poranne, M. Botoshansky, A. Stanger and E. Keinan, *Chem. Sci.*, 2020, **11**, 13015-13025.

58 G. Li, K. Xu, J. Zheng, X. Fang, W. Lou, F. Zhan, C. Deng, Y.-F. Yang, Q. Zhang and Y. She, *J. Am. Chem. Soc.*, 2024, **146**, 1667-1680.

59 J. Zhao, Q. Yang, W. Chen, N. Xu, Q. Zhang, W. Zhao, G.-G. Luo, Q. Cui and J. Huang, *Chem. Sci.*, 2025, **16**, 20445-20456.

60 M. S. Gordon, D. G. Fedorov, S. R. Pruitt and L. V. Slipchenko, *Chem. Rev.*, 2012, **112**, 632-672.

View Article Online
DOI: 10.1039/D6SC02521H

Crystallographic data for the structures reported in this article have been deposited at the Cambridge Crystallographic Data Centre, under deposition number 2486275 (**1c** at 0 °C), number 2486277 (**1c** at 60 °C), number 2486279 (**$2CH_3OH$·1c** at 0 °C). Copies of the data can be obtained free of charge via https://www.ccdc.cam.ac.uk/structures/. The experimental data and the characterization data are available in the Supplementary Information. All relevant data that support the findings of this work are available from the corresponding author on request. The atomic coordinates of the optimized computational model data generated in this study are provided in the Source Data file. Source data are provided with this paper.